Published in final edited form as:
Phys Med Biol. 2008 July 21; 53(14): 3723–3738. doi:10.1088/0031-9155/53/14/002.

Measured count-rate performance of the Discovery STE PET/CT scanner in 2D, 3D and partial collimation acquisition modes

L R MacDonald[1], **R E Schmitz**[1], **A M Alessio**[1], **S D Wollenweber**[2], **C W Stearns**[2], **A Ganin**[2], **R L Harrison**[1], **T K Lewellen**[1], and **P E Kinahan**[1]

1 *Department of Radiology, University of Washington, Seattle, WA 98195, USA*

2 *GE Healthcare, Waukesha, WI 53188, USA*

Abstract

We measured count rates and scatter fraction on the Discovery STE PET/CT scanner in conventional 2D and 3D acquisition modes, and in a partial collimation mode between 2D and 3D. As part of the evaluation of using partial collimation, we estimated global count rates using a scanner model that combined computer simulations with an empirical live-time function. Our measurements followed the NEMA NU2 count rate and scatter-fraction protocol to obtain true, scattered and random coincidence events, from which noise equivalent count (NEC) rates were calculated. The effect of patient size was considered by using 27 cm and 35 cm diameter phantoms, in addition to the standard 20 cm diameter cylindrical count-rate phantom. Using the scanner model, we evaluated two partial collimation cases: removing half of the septa (2.5D) and removing two-thirds of the septa (2.7D). Based on predictions of the model, a 2.7D collimator was constructed. Count rates and scatter fractions were then measured in 2D, 2.7D and 3D. The scanner model predicted relative NEC variation with activity, as confirmed by measurements. The measured 2.7D NEC was equal or greater than 3D NEC for all activity levels in the 27 cm and 35 cm phantoms. In the 20 cm phantom, 3D NEC was somewhat higher (~15%) than 2.7D NEC at 100 MBq. For all higher activity concentrations, 2.7D NEC was greater and peaked 26% above the 3D peak NEC. The peak NEC in 2.7D mode occurred at ~425 MBq, and was 26–50% greater than the peak 3D NEC, depending on object size. NEC in 2D was considerably lower, except at relatively high activity concentrations. Partial collimation shows promise for improved noise equivalent count rates in clinical imaging without altering other detector parameters.

1. Introduction

In positron emission tomography (PET), a 2D acquisition mode refers to the presence of photon-collimating septa between each axial detector ring. Fully 3D mode refers to the absence of all septa, with only end-shielding present to reduce detected events originating from outside the field of view. Fully 3D mode was introduced for its potential to improve effective count sensitivity. Removal of septa increases the detection rate of scattered and random coincidence counts as well as true coincidence counts. The benefits of 2D and 3D acquisition modes are dependent on several factors, most notably the activity distribution inside and outside the field of view of the scanner. The clinical use of fully 3D mode has demonstrated advantages over 2D mode in brain imaging (Dhawan *et al* 1998). Fully 3D mode is frequently used in whole-body PET scanning as well although the advantages of 3D over 2D mode for whole-body scanning are less well established (Raylman *et al* 1999, Brix *et al* 1999, Votaw *et al* 2001, Lartizien *et al* 2002, 2004). Whole-body imaging protocols and clinical tasks vary

E-mail: macdon@u.washington.edu.

considerably. Variables, such as injected dose, uptake time, body habitus, scan time, axial extent and clinical tasks, all have a role in optimizing a PET scan. This adds to the complexities of verifying distinct advantages of 2D versus 3D acquisition modes. Our group has previously studied the advantages of acquisition modes that use 'partial collimation', that is, a number of septa between those used for 2D and fully 3D modes (Schmitz *et al* 2007). In that work, Monte Carlo computer simulations were used to predict the count rates on an Advance PET scanner (GE Healthcare) for a wide variety of partial collimation modes. The results showed that noise equivalent count rates for the activity concentrations typically used in clinical settings could be increased over both 2D and 3D modes when using partial collimation configurations.

Much of the previous work on collimation in PET concerned the design of axial slats for coincidence imaging with dual-head gamma cameras (e.g. Joung *et al* (2002) and Rust and Kadrmas (2003)). The noise equivalent count (NEC) rate on these hybrid systems suffers due to the relatively low photo-electric cross section of the sodium iodide (NaI(Tl)) scintillation crystal at 511 keV. Low photo-electric cross section in the NaI(Tl) leads to a decrease in detected true coincidence events relative to scattered and random events. Count-rate limitations from ganged readout electronics also limit NEC. Optimizing axial slat configurations was studied extensively in order to reduce scatter and random coincidences in the hybrid systems. For full ring PET scanners, Tanaka *et al* (2000) used a novel approach of rotating 2D septa that covered only part of the detector ring transaxially, with the remainder uncollimated (3D). This allowed simultaneous 2D and 3D mode acquisition. This work focused on optimizing scatter and attenuation correction methods. Aykac, Baghaei and colleagues (Aykac *et al* 2002, Baghaei *et al* 2003) evaluated different septa designs on their prototype high-resolution PET module, using NEC as a figure of merit. They also conducted a detectability study for brain lesions. That work used the prototype module that was approximately 4 cm in axial extent and extrapolated results to a 13 cm axial system. The results showed increased NEC rates, but questionable improvement in brain lesion detectability. Hasegawa *et al* have constructed a custom PET scanner that is almost 70 cm in axial field of view (Hasegawa *et al* 2002, Ote *et al* 2003). They evaluated performance of this scanner using sparse septa. The long axial extent of the scanner suggested that some septa should be used to reduce the scattered and random coincidence events that would be experienced in fully 3D mode. However, they did not investigate optimal septa configurations, selecting instead to place septa between each detector block. This group focused on scatter correction techniques and image normalization in their analyses. In another look at partial collimation, Qi *et al* (2005) used simulations to systematically evaluate both NEC and the task of lesion detection for a prostate-optimized PET scanner. These studies evaluated the effect of the number of septa on both NEC rates and lesion detectability, and demonstrated that sparse septa can improve lesion detection over the complete absence of septa, or septa between all detector rings for this custom, application-specific design.

Our study of partial collimation is applied to a conventional clinical PET scanner focused on whole-body imaging. We continue to use the NEC metric as an indicator of imaging performance, as our previous studies have shown that lesion detection is closely related to NEC *density*, if all other parameters are kept constant (Kinahan *et al* 2005). Random coincidence counts and dead-time effects limit NEC in 3D mode with typical clinical activity concentrations in the field of view (FOV). In 2D, the NEC is limited by collimation; the system never reaches its count-rate potential at clinical activity levels. The goal of using the partial collimation configuration is to improve the statistically relevant count rates over 2D and fully 3D configurations for clinical activity concentrations, various patient sizes, and whole-body, as well as brain imaging.

In this study, we show that there is a predicted and measured improvement to NEC rates using partial collimation for the new GE Discovery STE (DSTE) PET/CT scanner geometry. The

DSTE scanner operates in either 2D or 3D mode, but with significantly shorter septa than those on the Advance; the septa length was reduced from 12 cm on the Advance to less than 6 cm on the Discovery STE. We used computer simulations and an empirical live-time function to first estimate count rates on the DSTE as a function of activity in a count-rate phantom. We then confirmed the predictions of our model with measured NEC in standard (2D and 3D) and partial collimation modes. This report thus also provides the NEMA NU2-2001 standard count-rate performance and scatter-fraction measurements from the DSTE PET/CT scanner.

2. Materials and methods

In our analysis the noise equivalent count rate (Strother *et al* 1990) is calculated from the true (T), random (R_{ROI}) and scattered (S_{ROI}) coincidence counts as

$$\mathrm{NEC}=\frac{T^2}{T+S_{\mathrm{ROI}}+R_{\mathrm{ROI}}} \tag{1}$$

where the ROI subscript indicates that we count only scattered and random events from within a region of interest (ROI) in the sinogram that contains events detected from the object being imaged. This form of NEC, also referred to as NEC(1R), is used when the random coincidences are calculated from single-photon event rates, as was done in this work. An alternative expression for NEC multiplies the random counts by a factor of 2 (NEC(2R)). NEC(2R) is used when measuring random events from a delayed coincidence window to take into account the added statistical noise of that measurement. Using scattered and random events from within an ROI is the method specified by the NEMA NU2 guidelines for noise equivalent count rate calculation. In particular, the NEMA standards state that the ROI is 24 cm across the projection dimension of the sinogram data, centered on the 20 cm diameter phantom.

Guided by the results from the work on the Advance scanner (Schmitz *et al* 2007), we pursued partial collimation modes that used one-half (‘2.5D’) and one-third (‘2.7D’) of the number of septa used in 2D mode on the DSTE scanner. Our scanner model was used to confirm similar relative increases in NEC for the DSTE as were predicted for the Advance. We then fabricated a set of 2.7D collimators for the DSTE and measured the count rate and scatter fraction according to the NEMA NU2 specifications. The count rates and scatter fraction measured in 2.7D mode were compared to the 2D and 3D measured results, and with the scanner model predictions.

2.1. Discovery STE PET/CT scanner

The first Discovery STE PET/CT scanner was installed at the University of Washington in September 2005. The DSTE PET scanner is a 24-ring bismuth germinate (BGO) system with 15.7 cm axial FOV and 70 cm transaxial FOV. The detector inner diameter is 88 cm. There are 560 BGO crystals in each ring. Individual BGO crystals are 4.7 mm × 6.3 mm × 30 mm (tangential × axial × radial). The DSTE is equipped with a retractable set of 23 tungsten septa, one between each of the 24 detector rings, plus end-shielding (figure 1(a)). The septa are 5.4 cm deep (radial dimension) and 0.8 mm thick. Approximately 7 mm of steel end-shielding is built into the collimator structure (figure 1(b)). Additional end-shielding exists in the mechanism that holds the collimators as well as behind the collimators (adjacent to the BGO).

Default data acquisition parameters on the DSTE differ in 2D and 3D. In 2D mode, events with energy between 375 and 650 keV are saved. In 3D the acceptance energy window is 425–650 keV. When binning the accepted coincident events into traditional 2D transaxial sinograms, the maximum allowable ring difference for a coincidence event is 5 for 2D, and 23 in 3D (i.e. coincidences between all rings are binned in 3D). The coincidence timing window is also different, being slightly wider in 2D mode (9.75 ns (3D) versus 11.05 ns (2D)).

Spatial resolution (FWHM) of the scanner is 5.1 mm in 2D mode and approximately 5.4 mm in 3D mode following NEMA NU2 standards (Kinahan *et al* 2006). System sensitivity is 2.2 counts s^{-1} kBq^{-1} in 2D and 8.4 counts s^{-1} kBq^{-1} in 3D.

2.2. Partial collimator 2.7D

A custom 2.7D partial collimator was constructed for the DSTE. The 2.7D collimator had the same geometry as the conventional 2D collimator, but with only seven septa. Figure 1(a) shows the axial distribution of the septa for 2D, 2.5D and 2.7D collimators. (The 2.5D case was modeled with simulations.) Figure 1(b) is a photograph of a 2.7D collimator segment next to a 2D collimator segment, showing the different septa patterns. The septa are installed on the DSTE in a series of collimator segments (figure 2).

2.3. Count-rate phantoms

The NEMA NU2 specified count-rate and scatter-fraction measurement uses a 20 cm diameter, 70 cm long polyethylene cylinder that is solid except for a 3 mm diameter hole along its length and 4.5 cm from the axis of the cylinder. A line source (18-F) is inserted into this hole and count rates are measured over time as the source activity decays.

The NEMA count-rate measurements were repeated with cylinders of 27 cm and 35 cm diameters in order to study how noise equivalent count rates change with increased scatter medium. We are interested in these larger phantoms because the standard 20 cm diameter phantom is not representative of all patient sizes seen in clinical PET scanning. In each case, the larger diameter cylinders were still 70 cm long, and the same source position was used, i.e., the source was a 70 cm long, 3 mm diameter line source displaced 4.5 cm from the cylinder axis.

The NEMA NU2 prescription for calculating count rates and scatter fraction uses a 24 cm wide ROI in the sinogram for all view angles, centered on the 20 cm diameter phantom. We extended this definition for the larger diameter phantoms by keeping the ROI 4 cm wider than the object. Hence, the ROIs for the 27 cm and 35 cm diameter phantoms were 31 cm and 39 cm wide.

2.4. SimSET Monte Carlo simulation

We modeled DSTE count rates with the SimSET Monte Carlo photon-tracking program (Lewellen *et al* 1998) in 2D, 2.5D, 2.7D and 3D modes. One simulation run tracked true and scattered coincidence events. These were histogrammed according to the DSTE detector geometry. To estimate random coincidence rates, we ran SimSET in a mode that allowed tracking single photons, instead of coincidence photon pairs. This gave an estimation of the detected singles events, from which we calculated random events (Stearns *et al* 2003). A third simulation run tracked and recorded single photons down to very low energies. These photons were binned according to energy, rather than by individual crystal, as in the single-photon run used to calculate random coincidences. This ‘trigger singles’ run was used to determine incident photon flux rates that were needed to predict scanner live time, as described later in this section. It was necessary to separate the single-photon runs in order to maintain a reasonable output data file size. The data files would have been unwieldy if photons were binned according to both individual crystal (13 440 in all) and by energy.

The PET scintillation crystals were modeled as a solid annulus of BGO in the simulations. This differs from the scanner construction, which employs block detectors (Casey and Nutt 1986). This results in several important differences between the Monte Carlo model and the physical scanner. One is the total volume of scintillation material. We corrected the simulation output by a packing-fraction factor representing the difference in the BGO volume of the solid annulus and the actual volume of BGO in the DSTE scanner. The volume of BGO in the DSTE is

calculated from the specifications given in section 2.1. The volume of BGO in the simulation is calculated from an annulus with an inner diameter of 88 cm, an outer diameter of 94 cm (3 cm thick BGO) and an axial extent of 15.5 cm. The packing fraction was found to be 88.7%. Count losses due to inter-block scattering and event mispositioning are two other factors that are difficult to estimate without accurately tracking photons through detector block structures.

An estimation of the count losses from system dead time is necessary in order to find the NEC curves as a function of activity in the FOV. We used an empirical method for predicting live-time count losses for partial collimation. Count losses as a function of activity were measured in 2D and 3D modes. These live-time curves were then generalized to partial collimation mode by matching trigger singles rates in different acquisition modes. This assumed that the primary determining factor of the live-time fraction was the incident photon flux that triggers the system to begin processing events. Details of the different components of the readout circuits that contribute to dead time were not explicitly modeled, but rather modeled together as a global parameter based on the measured live-time fractions.

There are inevitably differences in data collection and processing methods for 2D and 3D acquisition modes. These differences originate from the significant changes in incident photon flux and number of lines-of-response between the two modes of acquisition. Partial collimation presents a new acquisition mode for which optimal acquisition and processing parameters must be determined. For example, partial collimation introduces new sensitivity variations in the axial dimension due to the new pattern of septa placement. The axial sensitivity also depends on how data are saved and binned. The default data binning routines on the DSTE use a maximum ring difference of 5 in 2D (using single-slice rebinning (Daube-Witherspoon and Muehllehner 1987)) and 23 in 3D (using 3D reconstruction methods). An obvious drawback of accepting events from a limited number of ring differences is the corresponding reduction in count sensitivity. To study this reduction for the partial collimation modes, we used single-slice rebinning with various maximum ring differences and calculated the peak NEC value for each case. Ultimately, the choice of maximum ring difference should depend on the tradeoffs between sensitivity, computational load and spatial distortions (if SSRB is used) and is beyond the scope of this study.

2.5. Scanner measurements

The collimator is a major component of any clinical PET scanner that is equipped with septa. Unlike gamma cameras, PET systems are not designed for collimator switching. If the system has the option of operating in either 2D or 3D modes, then a retraction mechanism behind the system covers moves the collimators in line with the detectors (2D mode) or completely out of the FOV (3D mode). There is no means of removing a select number of septa from the collimator. Custom 2.7D collimators had to be manufactured and installed in place of the 2D collimators. Figure 1(b) shows the standard 2D septa next to the custom 2.7D septa. Figure 2 shows the DSTE system with the covers off and collimator segments being installed.

In addition to the mechanical switching of the collimators, the system configuration protocols required modification in order to acquire data using 3D mode parameters while the collimator mechanism was in place. A combination of switches, relays and configuration files signals the DSTE to acquire with 2D mode parameters when the collimator is in front of the detectors. A new system configuration was developed for acquiring data with 3D mode parameters (e.g. 3D data binning, energy window and timing window) when the 2.7D collimator was in front of the detectors. Calibration routines, such as collimator alignment and absolute activity conversion factors, had to be established for the 2.7D measurements. We also collected normalization data for use in image reconstruction tasks.

The NEMA NU2 protocols were followed for conventional 2D and 3D count-rate and scatter-fraction measurements on the DSTE. These measurements consist of filling the line source with activity well above typical clinical levels (~900 MBq for 3D, ~2500 MBq for 2D) and then recording events at several time points during the source decay. The final acquisition is performed at an activity with an insignificant random coincident count rate. We then replaced the 2D collimator with the 2.7D collimator. The same NEMA protocols were followed using partial collimation for the three different phantom diameters. The energy window was 425–650 keV and data were binned using coincidence events between all detector rings (maximum ring difference = 23) for the measured 2.7D data.

3. Results

3.1. SimSET Monte Carlo simulations

The maximum NEC was studied as a function of the maximum ring difference used in data rebinning. We found an increase in NEC with increasing maximum ring difference, with the highest NEC occurring when binning events between all detector rings (max. ring difference = 23). This was expected because lines-of-response between all detector rings are possible in the 2.5D and 2.7D septa configurations. Figure 3 shows how the peak NEC changed with maximum ring difference. (Note that the septa were modeled as tungsten in SimSET, so septa penetration effects are included in the simulation results.)

There is a diminishing increase in NEC as the maximum ring difference is increased. This was also expected since there are fewer possible lines-of-response between widely separated rings. Peak NEC fell by approximately 5% when limiting the maximum ring difference to 15 and 17 for 2.5D and 2.7D, respectively. This information is useful when deciding whether data between all 24 rings should be saved. Without having evaluated all the information needed to determine the best clinical implementation of these partial collimation modes as discussed above, we elected to use the maximum possible ring difference of 23 when processing the partial collimation data. This approach provides the most direct comparison to 3D mode acquisition. All of the data analysis in this paper uses a maximum ring difference of 5 for 2D and 23 for 2.5D, 2.7D and 3D. In keeping the partial collimation data consistent with 3D acquisition mode, we also used the default 3D energy window and coincidence timing window for partial collimation simulation and acquisition.

Figure 4 shows the axial variation in singles and true coincidence counts for all collimation modes from the 20 cm diameter phantom.

Axial variations in counts are expected from the placement of the septa. The patterns seen in figure 4 follow from the collimation configurations and data binning. Accounting for these sensitivity variations is part of the data normalization process in image reconstruction.

The count sensitivities given in figure 4 do not account for dead-time count losses or changes due to event mispositioning at high count rates. The simulated data were adjusted according to the live-time model in order to estimate counts as a function of activity in the phantom. Apart from the live-time factor, and the packing-fraction factor mentioned earlier, no further modifications were made to the simulated data presented here. The modeled true, scattered, random and NEC event rates as a function of the activity in the 20 cm diameter phantom for each collimation configuration are shown in figure 5.

The count-rate variation is shown up to 1500 MBq in the phantom, even though the activity injected into patients is less than 1000 MBq, and more commonly in the 370–740 MBq range. In FDG oncology imaging, the tracer is usually allowed to distribute for 45–60 min before scanning, reducing the typical activity range at scan time to 250–550 MBq. One goal of the

NEMA NU2 count-rate experiment is to measure the activity at which these count rates reach their limit and begin to decrease. As mentioned in the introduction, and reflected in figure 5 (d), the maximum 2D NEC occurs above clinical activity levels, while the 3D NEC peaks at or below typical clinical activity. The 3D NEC curve is characterized by a rapid decline beyond its peak. Conversely, 2D NEC is slow to reach its peak. The 2D and 3D NEC curves cross at about 500 MBq, which is in the clinical range of injected activity. While figure 5 represents modeled results from a particular scanner, the trends just described apply in a general sense to all full ring PET scanners. Figure 5(d) clearly shows the potential benefits of partial collimation to the NEC rate in this context; not only do the partial collimation NEC rates reach a higher value overall, they achieve this advantage in the activity range most commonly used in clinical PET scanning.

Figure 5 shows results from the 20 cm diameter phantom. However, it is safe to say that this object is not an accurate representation of typical patient size. The NEC curves predicted by our model for the larger phantoms are shown in Figure 6.

Figure 6 shows that NEC is reduced overall for larger phantom diameters (cf figure 5(d)). The relative advantages of partial collimation are maintained for the larger phantoms. In fact, the slight advantage of 3D NEC below ~240 MBq for the 20 cm phantom is reduced in the larger phantoms.

3.2. Measured count rates

Experimental complexities forced us to select one of the partial collimation configurations for testing on the scanner. The NEC curves in figures 5(d) and 6 show 2.5D NEC has a slightly higher peak value, but at the high end of the clinical activity range. The 2.7D NEC is slightly higher at low activity. There is no clear distinguishing feature. We selected 2.7D since it is closer to 3D, which is the predominant acquisition mode used in PET.

The measured 2D, 2.7D and 3D true, scattered and random count rates as a function of activity in the 20 cm diameter cylinder are shown in figure 7.

The shapes of the measured true and scattered count-rate curves (figure 7) follow the predictions by the simulation studies (figure 5) in that the peaks occur at nearly the same activity. The simulated data overestimated both true and scattered events. The overestimation of true counts ranged between 25 and 40% depending on collimation and phantom size. We were unable to determine trends in the error to help identify possible sources of the discrepancy. Scatter was overestimated more for 3D (~40%) than other modes (~10%). The higher rate of scatter detection in 3D mode may contribute to this trend. Random events were predicted very well (within 5%), indicating that the singles rates were modeled well by the simulation.

Figure 8 shows the NEC curves calculated from the above measurements for different phantoms sizes and collimation modes. (The 27 cm phantom was not measured in 2D.)

The measured NEC results also follow the trends predicted by the simulation results. Since NEC is calculated from the true, scattered and random events, discrepancies between the modeled and measured NEC originate from those quantities. The shape of the NEC curve is determined by where the true and scattered event rates begin to decline and the rise of the randoms curve. Since the turnover of the true and scattered events was predicted by the model, and the randoms were accurately predicted, the shape of the modeled NEC curve is a good match to the measured results. Table 1 gives the measured and modeled peak NEC, and activity at which NEC peaked, for the experiments described in this paper.

The measurements yielded a greater relative improvement in 2.7D peak NEC over 3D than the model predicted. For the 20 cm phantom, the model predicted that 2.7D peak NEC would be 17% greater than 3D peak NEC. The measured 2.7D peak NEC was 26% higher. The model predicted 2.7D peak NEC to be 32% and 35% above 3D for the 27 cm and 35 cm phantoms, respectively. The measured improvements were 42% and 50%, respectively.

The relative fraction of scattered events increases when there are fewer septa and for the larger phantoms. Table 2 lists the scatter fraction for the different size phantoms and different collimators, from both measured and simulated results. Scatter fraction is defined as

$$\text{scatter fraction} = \frac{S_{\text{ROI}}}{T + S_{\text{ROI}}}. \tag{2}$$

Greater overestimation of the relative number of true events in the simulation studies leads to an underestimation of the scatter fraction from the simulation results. We suspect that the lack of detailed detector block modeling is responsible for overestimating true events. Scatter fractions follow expected trends and represent another benefit of partial collimation over fully 3D acquisition.

4. Discussion

The use of septa in PET scanners dates back to early scanner design when it was important to limit count rates and dataset size, and transaxial slices were a natural way to acquire data given other axial tomography technology and conventional reconstruction methods. Over time, the practice of removing the septa has been adopted, which increases the tomograph sensitivity, potential dataset size and imposes new demands on normalization and image reconstruction. The NEC rate of a PET system without any septa (3D acquisition mode) is greater than NEC with septa between every detector ring (2D mode) for low and medium activities in the patient. At higher activities, the random event rate becomes prohibitive in 3D (thus degrading NEC rates), and 2D mode becomes superior from an NEC point of view. The activity concentration at which 2D NEC surpasses 3D NEC depends on injected dose and patient size and is frequently in a range commonly used in clinical PET imaging, thus creating an ambiguity as to the preferable acquisition mode. Partial collimation is appealing because it offers a way to balance the advantages and disadvantages of 2D and 3D acquisition: random events are substantially reduced compared to 3D, without the large loss of true event sensitivity seen in 2D. We have shown that partial collimation can lead to an NEC rate greater than in 2D and 3D modes for activity ranges typically used in clinical scanning.

We have constructed and installed partial collimators on a commercial clinical PET scanner as a means of increasing NEC rates without altering other detector properties or parameters. Previous investigations into using sparse septa have focused on hybrid scanners, custom, prototype ring systems or computer simulation results. The work on full ring or ring-type tomographs (Aykac *et al* 2002, Baghaei *et al* 2003, Hasegawa *et al* 2002, Ote *et al* 2003, Qi *et al* 2005) demonstrated NEC advantages when using collimation between 2D and fully 3D. Investigation into advantages of partial collimation for lesion detectability (Baghaei *et al* 2003, Qi *et al* 2005) showed mixed results for the clinical tasks studied (brain, prostate).

In this paper we focused on the NEMA NU2 prescribed count-rate and scatter-fraction measurement. The NEMA NU2 standard specifies the count-rate phantom, activity, imaging protocol and how acquired data are to be analyzed. However, the specifics of data acquisition and processing methods on a particular scanner are left to the investigator (data binning, energy window and coincidence window). There are several differences between how data are collected and processed in 2D and 3D modes for the DSTE PET/CT scanner. After studying

peak NEC rates as a function of maximum accepted ring difference (figure 3), we elected to use the 3D mode parameters for the analysis of partial collimation data.

The effort required to configure the DSTE scanner for partial collimation limits our access to measured partial collimation data. The NEC rates predicted by the scanner model were nearly equivalent for 2.5D and 2.7D collimation. We considered 2.7D to be marginally better, so we chose to measure count rates using 2.7D collimators. We measured count rates in the NEMA NU2 count-rate phantom as a starting point for evaluating the statistical quality of acquired data. The NEMA NU2 count-rate phantom does not contain activity distributed throughout an extended volume, as is the case in patients. The NEC density has been shown to be an accurate predictor of image quality (Kinahan *et al* 2005) if all other factors are held constant, so we believed this to be the appropriate starting point for evaluating partial collimation data. An essential next step is the evaluation of task-based metrics of image quality, especially using images with anthropomorphic activity distributions.

The absolute true and scattered coincidence event rates predicted by simulations were above measured rates (differences were between 25 and 40%, depending on collimation and phantom size). In our scanner model, we corrected for bulk BGO crystal volume difference, and adjusted output counts for dead-time factors, but no further adjustments were made. The discrepancy in count rate is attributable in part to the absence of block detector modeling in the current version of SimSET. Also absent from the simulation model is the patient bed. We expect the bed to have a small effect on global count rates. We found random coincidence rates to be predicted quite well (within 5%) by the model. Random rates were calculated from single-photon events, indicating that the single-photon detections were accurately modeled. Thus far we have not been able to identify consistent multiplicative factors that scale our SimSET results to measured data. SimSET continues to undergo development in our laboratory.

The measured partial collimation count rates confirmed the advantages predicted by our scanner model. The model predicted where the 2.7D mode NEC would peak relative to the 2D and 3D NEC peaks (figures 5(d), 6 and 8, and table 1). Measurements also verified that 2.7D peak NEC is greater than 2D and 3D peak NEC. The activity at which 2.7D NEC reached its peak was 400–500 MBq, which is very well suited to clinical PET imaging. At activities below this, the measured 2.7D NEC rate was as high as 3D NEC for the 27 cm and 35 cm phantoms, and only slightly lower in the 20 cm phantom. This was also predicted by the model. Based on these results, for optimal NEC rate, the 2.7D collimation configuration is preferable to conventional PET acquisition modes for a wide variety of object sizes and all relevant activities.

Our tests were performed with relatively simple phantoms in which the activity was concentrated in a line, rather than distributed throughout the volume of the object. Table 1 shows that NEC rates peak at approximately the same activity level, regardless of phantom size. If we consider the NEC curves as a function of activity *per unit volume of scatter medium* (activity *concentration*), then the peak NEC occurs at lower activity concentrations for larger objects. The volumes of the three phantoms tested here are ~22 L (20 cm φ), ~40 L (27 cm φ) and ~67 L (35 cm φ). The 2.7D peak NEC occurs at ~25 kBq mL^{-1}, ~14 kBq mL^{-1} and ~8 kBq mL^{-1} in the 20 cm, 27 cm and 35 cm phantoms, respectively. The activity concentration at which peak NEC occurs for other collimations relative to 2.7D are maintained for each phantom size (i.e. lower for 3D, higher for 2.5D and 2D). The activity concentration in a 70 kg person injected with 500 MBq is ~7 kBq mL^{-1} (assuming 70 kg corresponds to 70 L). This again shows that the 2.7D peak NEC occurs near a common clinical activity concentration (peak NEC at ~8 kBq mL^{-1} in a 67 L object, compared to typical ~7 kBq mL^{-1} in 70 L patient). The largest phantom used in our experiments, ~67 L, is still smaller in volume than an average adult (~70 kg). However, the analysis in terms of activity concentration

is limited by the fact that (1) the activity is not distributed irregularly throughout the volume of scatter medium in our experiments and (2) the phantoms are not the same shape as people.

In certain PET imaging protocols, such as cardiac imaging and other gated or dynamic protocols, activity at scan time is considerably higher than typical oncology imaging protocols. For these studies 2D mode can be preferable from an NEC standpoint. Fully 3D mode NEC rates fall rapidly after peaking (figure 8) and 2D NEC rates are higher in the high activity range of interest. In addition to large random coincidence event rates, and count losses due to dead time, event mispositioning due to pulse pileup can significantly degrade image quality at high activity. For these high-dose applications partial collimation NEC rates are increased relative to what can be achieved in either 2D or 3D acquisition modes.

Partial collimation introduces new axial sensitivity variations on the acquired data. Figure 4 shows that axial variations exist in 2D and 3D modes as well. It is part of the data normalization process to correct for these variations before or as part of the image reconstruction. The partial collimation axial variations have a more irregular pattern. We have acquired normalization scans with the 2.7D collimator using a sheet source for purposes of investigating reconstruction of data acquired in partial collimation mode (Alessio *et al* at press).

5. Conclusions

We have demonstrated two benefits of partial collimation: increased peak NEC count-rate values and increased NEC rates over a wider range of clinical activity levels. The measured peak NEC in 2.7D was 26%, 42% and 50% higher than 3D peak NEC for the NEMA NU2 count-rate phantoms of 20 cm, 27 cm and 35 cm diameters, respectively. Peak NEC rates in 2.7D mode were measured to be ~10% greater than in 2D mode for the 20 cm and 35 cm phantoms. Equally important is the fact that 2.7D NEC peaked near the mid-range of activities most commonly used in clinical PET imaging (~400–500 MBq). Furthermore, unlike in 2D mode, 2.7D mode NEC rates were as high as 3D mode NEC rates at low activities (figure 8). This satisfies one of the primary goals of this work, which was to extend the high NEC rates obtained in 3D mode to higher activity levels, without losing the advantage of high NEC at low activities. Partial collimation therefore stands to improve the statistical quality of many standard patient scans. Partial collimation on clinical PET scanners merits further investigation using objective measures of task performance (e.g. measuring lesion detection).

Acknowledgements

This work was supported in part by the US National Institutes of Health under grant nos CA042593 and CA74135, and by General Electric Healthcare Technologies. The authors wish to thank the anonymous reviewers of this article for their constructive commentary and suggestions.

References

Alessio AM, Schmitz RE, MacDonald LR, Wollenweber SD, Stearns CW, Ross SG, Ganin A, Lewellen TK, Kinahan PE. Image reconstruction for a partially collimated whole body PET scanner. IEEE Trans Nucl Sci :55.

Aykac M, Uribe J, Baghaei H, Li H, Wang Y, Liu Y, Xing T, Wong W-H. Septa design study for volumetric imaging in positron emission tomography. IEEE Trans Nucl Sci 2002;49:2097–102.

Baghaei H, Wong W-H, Uribe J, Li H, Aykac M, Wang Y, Liu Y, Xing T, Farrel R. Brain lesion detectability studies with a high resolution PET operation in no-septa and partial-septa configurations. IEEE Trans Nucl Sci 2003;50:1364–9.

Brix G, Adam LE, Zaers J, Trohan H, Bellemann ME, Mosske D, Doll J. Reduction of radiation exposure in PET examinations by data acquisition in the 3D mode. Nuklearmedizin 1999;38:75–9. [PubMed: 10320992]

Casey ME, Nutt R. A multi-crystal two dimensional BGO detector system for positron emission tomography. IEEE Trans Nucl Sci 1986;33:460–3.

Daube-Witherspoon ME, Muehllehner G. Treatment of axial data in 3D PET. J Nucl Med 1987;28:1717–24. [PubMed: 3499493]

Dhawan V, Kazumata K, Robeson W, Belakhlef A, Margouleff C, Chaly T, Nakamura T, Dahl R, Margouleff D, Eidelberg D. Quantitative brain PET. Comparison of 2D and 3D acquisitions on the GE advance scanner. Clin Positron Imaging 1998;1:135–44. [PubMed: 14516603]

Hasegawa T, Tanaka E, Yamashita T, Watanabe M, Yamaya T, Murayarna H. A Monte-Carlo simulation study on coarse septa for scatter correction in 3D PET. IEEE Trans Nucl Sci 2002;49:2133–8.

Joung J, Miyaoka RS, Kohlmyer SG, Harrison RL, Lewellen TK. Slat collimator design issues for dual-head coincidence imaging systems. IEEE Trans Nucl Sci 2002;49:141–6.

Kinahan, PE.; Cheng, P.; Alessio, AM.; Lewellen, TK. A quantitative approach to a weight-based scanning protocol for PET oncology imaging. IEEE Nucl. Sci. Symp. and Medical Imaging Conf. (Puerto Rico); 2005. p. 1886-90.

Kinahan PE, et al. 2006 Performance evaluation of an integrated PET/CT scanner: discovery STE. J Nucl Med 47:392P.(abstract)

Lartizien C, Comtat C, Kinahan PE, Ferreira N, Bendriem B, Trebossen R. Optimization of injected dose based on noise equivalent count rates for 2- and 3-dimensional whole-body PET. J Nucl Med 2002;43:1268–78. [PubMed: 12215569]

Lartizien C, Kinahan PE, Comtat C. A lesion detection observer study comparing 2D versus fully-3D whole-body PET imaging protocols. J Nucl Med 2004;45:714–23. [PubMed: 15073270]

Lewellen, TK.; Harrison, RL.; Vannoy, S. The SimSET Program in Monte Carlo Calculations in Nuclear Medicine. Ljungberg, M.; Strand, S.; King, M., editors. Philadelphia, PA: Institute of Physics Publishing; 1998. p. 77-92.

Ote, K.; Takahashi, M.; Kosugi, T.; Yamada, R.; Watanabe, M.; Yamashita, T.; Hasegawa, T.; Tanaka, E. Data correction and normalization for a new PET scanner having coarse septa. IEEE Nuclear Science Symp. Conf. Record (IEEE Cat. No.03CH37515); 2003. p. 2420-4.

Qi J, Huber JS, Huesman RH, Moses WW, Derenzo SE, Budinger TF. Septa design for a prostate specific PET camera. IEEE Trans Nucl Sci 2005;52:107–13.

Raylman RR, Kison PV, Wahl RL. Capabilities of two- and three-dimensional FDG-PET for detecting small lesions and lymph nodes in the upper torso: a dynamic phantom study. Eur J Nucl Med 1999;26:39–45. [PubMed: 9933660]

Rust TC, Kadrmas DJ. Survey of parallel slat collimator designs for hybrid PET imaging. Phys Med Biol 2003;48:N97–104. [PubMed: 12699197]

Schmitz RE, Harrison RL, Stearns CW, Lewellen TK, Kinahan PE. Optimization of noise equivalent count rate performance for a partially collimated PET scanner by varying the number of septa. IEEE Trans Med Imaging 2007;26:935–44. [PubMed: 17649907]

Stearns CW, McDaniel DL, Kohlmyer SG, Arul PR, Geiser BP, Shanmugam V. Random coincidence estimation from single event rates on the discovery ST PET/CT scanner. Proc IEEE Nuclear Science Symp/Medical Imaging Conf 2003;5:3067–9.

Strother SC, Casey ME, Hoffman EJ. Measuring PET scanner sensitivity: relating count rates to image signal-to-noise ratios using noise equivalent counts. IEEE Trans Nucl Sci 1990;37:783–8.

Tanaka E, Hasegawa T, Yamashita T, Okada H, Murayama H. A 2D/3D hybrid PET scanner with rotating partial slice-septa and its quantitative procedures. Phys Med Biol 2000;45:2821–41. [PubMed: 11049174]

Votaw JR, White M. Comparison of 2-dimensional and 3-dimensional cardiac 82Rb PET studies. J Nucl Med 2001;42:701–6. [PubMed: 11337563]

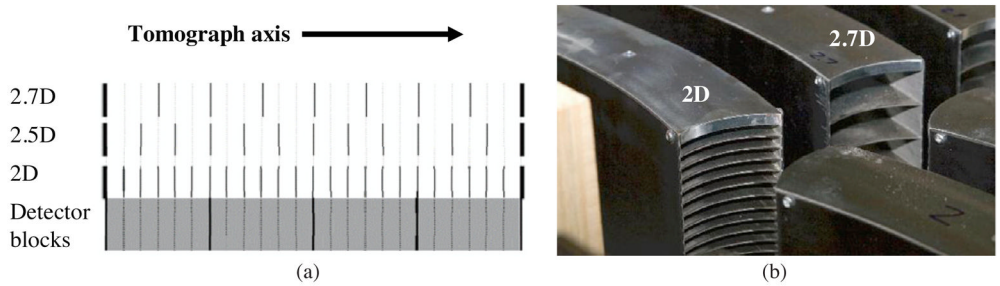

Figure 1.

(a) Axial placement of the septa (thin vertical lines) in partial collimation modes. The thick vertical lines at either end indicate end-shielding. There are four detector blocks axially, each with six crystals along the axis. The image is not to scale. (b) Individual collimator segments for the 2D and 2.7D collimators. The thicker end shields are evident on top.

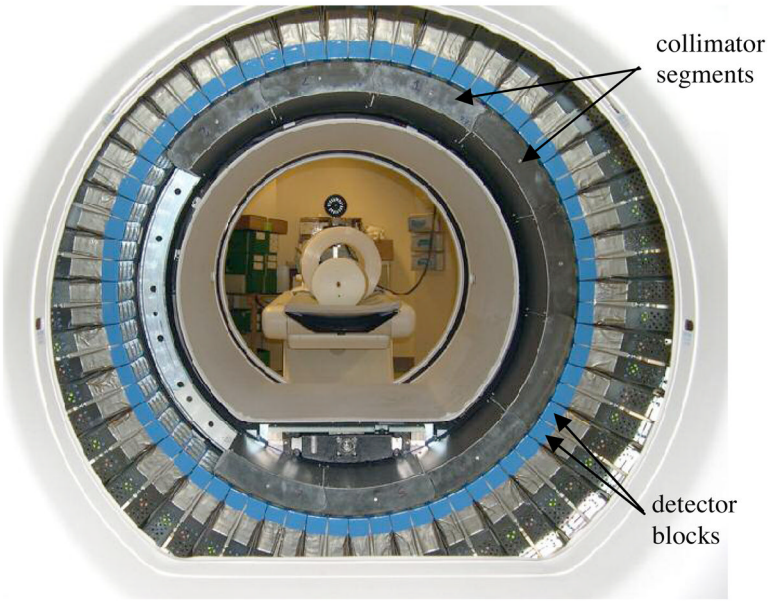

Figure 2.
The DSTE scanner ring with collimator segments being installed. The collimator segments are missing near the 9 o'clock position viewing this photo. Nine collimator segments are installed around the rest of the ring. Behind the detector ring, the NEMA count-rate phantom is seen on the patient table. Behind the cylinder phantom is the sheathing for making larger diameter phantoms.

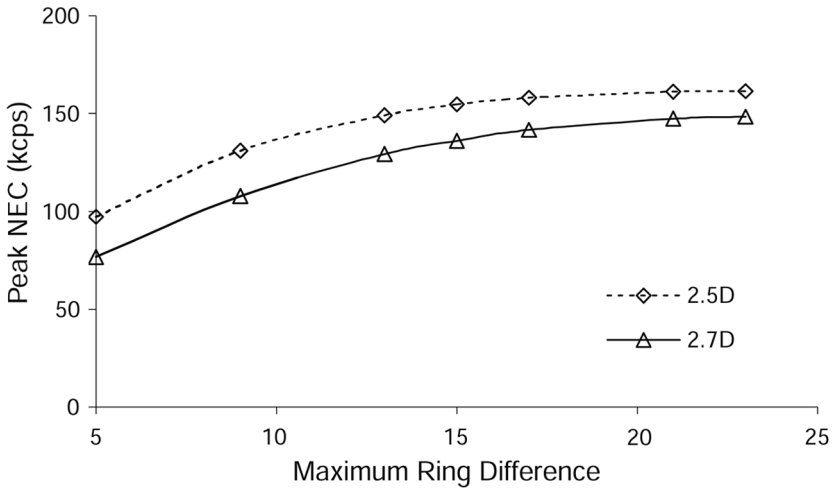

Figure 3.
Simulated data from the 20 cm diameter phantom were binned into 47 transaxial slices using different maximum ring differences in the binning algorithm. The total NEC from the entire scanner was calculated for each case, and the variation in total NEC with maximum ring difference is shown here for 2.5D and 2.7D collimation.

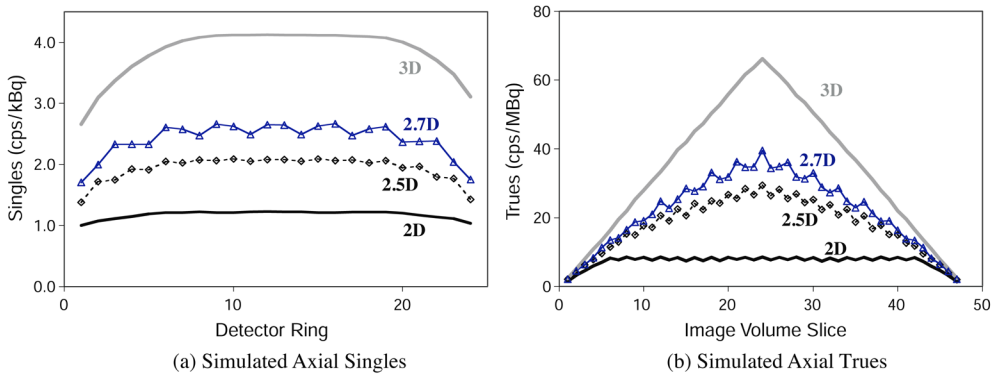

Figure 4.

Simulated single-photon event rates and true (unscattered) coincidence event rates in the 20 cm diameter phantom as a function of axial slice. Coincidence data were binned using single-slice rebinning; maximum accepted ring difference was 5 for 2D, and 23 for 2.5D, 2.7D and 3D. (a) Singles. (b) Trues.

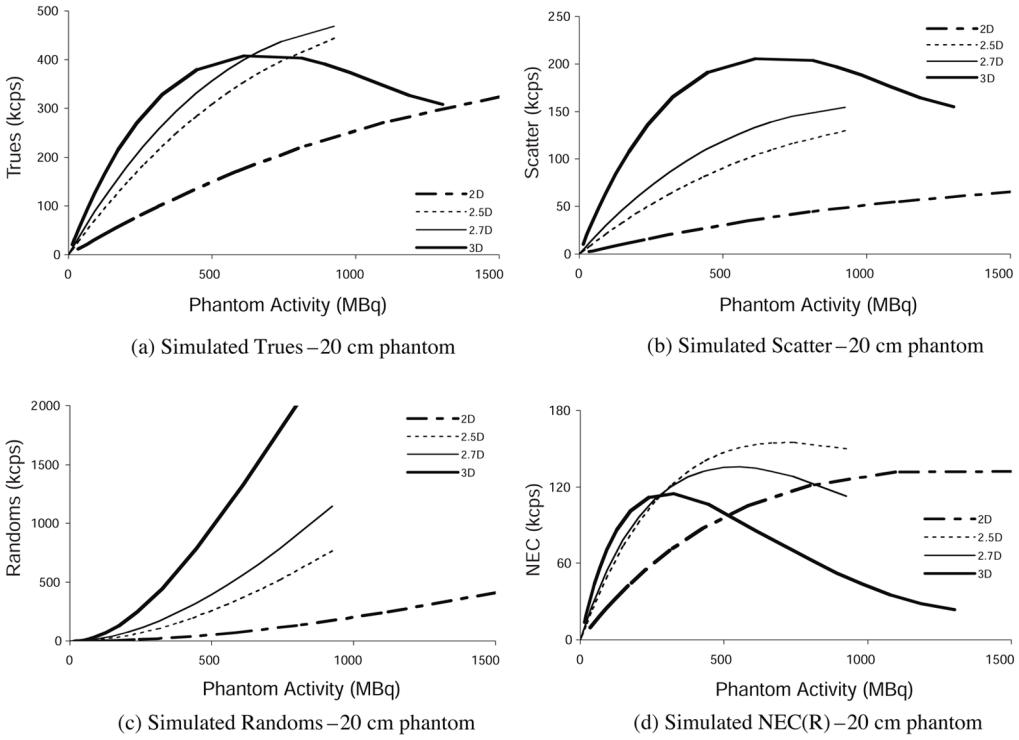

(a) Simulated Trues – 20 cm phantom

(b) Simulated Scatter – 20 cm phantom

(c) Simulated Randoms – 20 cm phantom

(d) Simulated NEC(R) – 20 cm phantom

Figure 5.

Simulated results: (a) true, (b) scattered, (c) random and (d) NEC event rates versus activity in the 20 cm diameter NEMA count-rate cylinder phantom for each septa configuration.

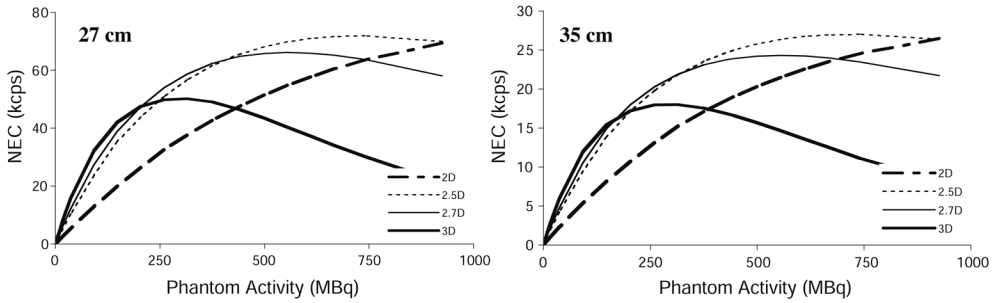

Figure 6.
NEC rates from simulated data for the 27 cm diameter phantom (left) and the 35 cm diameter phantom (right) for all collimation modes. Note changes in scale.

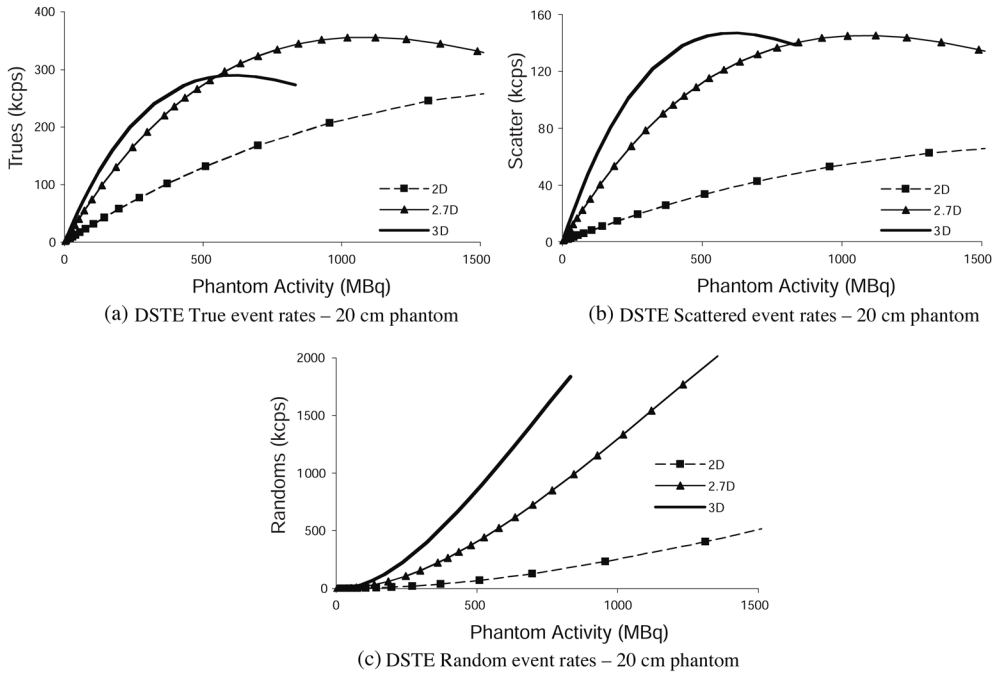

Figure 7.
Coincidence count rates measured on the DSTE PET scanner: (a) trues, (b) scattered and (c) randoms.

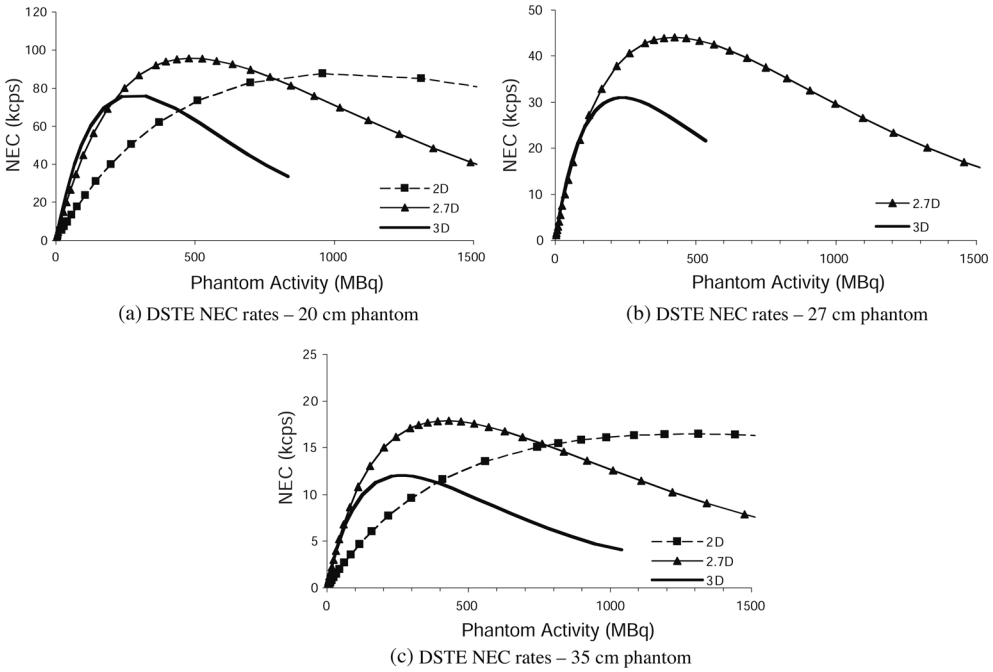

Figure 8.

Measured noise equivalent count rates using 2D, 2.7D and 3D modes for different cylinder sizes: (a) 20 cm phantom, (b) 27 cm phantom and (c) 35 cm phantom. The 27 cm phantom was not measured in 2D.

Table 1

Peak NEC.

		Simulated		Measured	
		Peak NEC (kcps)	**Activity of peak NEC (MBq)**	**Peak NEC (kcps)**	**Activity of peak NEC (MBq)**
2D	20 cm	132	1291	88	957
	27 cm	69[a]	925	*b*	*b*
	35 cm	26[a]	925	16	1312
2.5D	20 cm	155	725	*b*	*b*
	27 cm	72	723	*b*	*b*
	35 cm	27	724	*b*	*b*
2.7D	20 cm	135	555	96	476
	27 cm	66	555	44	425
	35 cm	24	555	18	428
3D	20 cm	115	317	76	280
	27 cm	50	314	31	240
	35 cm	18	286	12	290

[a] Peak NEC was not reached in the activity range simulated.

[b] Measurements corresponding to these cells were not made.

Table 2

Scatter fraction derived from measurements and simulations.

	2D		2.5D	2.7D		3D	
	Simulated	**Measured**	**Simulated**	**Simulated**	**Measured**	**Simulated**	**Measured**
20 cm	16.8	20.3	22.6	26.0	29.0	33.5	33.7
27 cm	17.7	[a]	31.7	35.7	38.9	42.6	45.3
35 cm	25.3	34.4	40.9	45.7	46.6	53.3	54.8

[a] 2D 27 cm case was not measured.